Available online at www.sciencedirect.com
SCIENCE DIRECT®
ELSEVIER
Ultramicroscopy 102 (2005) 317–326
ultramicroscopy
www.elsevier.com/locate/ultramic

The spatial resolution of imaging using core-loss spectroscopy in the scanning transmission electron microscope

E.C. Cosgriff[a], M.P. Oxley[a], L.J. Allen[a,*], S.J. Pennycook[b]

[a]*School of Physics, University of Melbourne, Vic. 3010, Melbourne, Australia*
[b]*Oak Ridge National Laboratory, Condensed Matter Sciences Division, P.O. Box 2008, Oak Ridge, TN 37831-6030, USA*

Received 26 July 2004; received in revised form 5 November 2004; accepted 12 November 2004

Abstract

The 'delocalization' of inelastic scattering is an important issue for the ultimate spatial resolution of core-loss spectroscopy in the electron microscope. This paper investigates the resolution of scanning transmission electron microscopy images for single, isolated atoms. Images are simulated from first principles using a nonlocal model for electron core-loss spectroscopy. The role of the width of the probe relative to the delocalization of the underlying ionization interaction is considered.
© 2004 Elsevier B.V. All rights reserved.

Keywords: Delocalization of inelastic scattering; Core-loss spectroscopy; Scanning transmission electron microscopy

1. Introduction

In recent years, atomic resolution microscopy has become an essential tool in areas such as nanotechnology [1] and bioengineering. Its uses include the investigation of the properties of materials containing dopants and the characterization of biological samples [2]. The scanning transmission electron microscope (STEM) is able to provide images at atomic resolution, the more so if fitted with a field emission gun (FEG) and a spherical aberration corrector.

The advent of aberration correctors for STEM probe forming optics allows third-order spherical aberration as well as defocus to be varied [3,4]. These aberrations can then be used to offset the effect of fifth-order spherical aberration in order to obtain an aberration balanced probe which approximates an aberration free probe. The reduction in coherent aberrations allows the aperture of the probe forming optics to be increased in size, resulting in a smaller probe [5]. The availability of aberration correctors has led to a rapid increase in resolution in electron microscopy, as manifested, for example, in the UK

*Corresponding author. Tel.: +61 3 8344 7402; fax: +61 3 9347 4783.
E-mail address: lja@physics.unimelb.edu.au (L.J. Allen).

0304-3991/$ - see front matter © 2004 Elsevier B.V. All rights reserved.
doi:10.1016/j.ultramic.2004.11.001

SuperSTEM and the Department of Energy transmission electron aberration-corrected microscope (TEAM) projects [6,7]. Aberration corrected STEMs operating at 100 keV can routinely produce STEM probes of approximately 1 Å in size. Small probe sizes have led to successful detection of single atoms on the surface or within bulk samples [8,9]. Increasing the energy of electrons within the probe to 300 keV leads to a reduced wavelength and the possibility of forming even finer probes, such as in the VG Microscopes HB603U STEM at Oak Ridge National Laboratory (fitted with a NION aberration corrector). All calculations in this paper are done assuming 300 keV incident electrons.

Annular dark field (ADF) images are produced by electrons which have undergone thermal diffuse scattering (TDS). The intensity of these incoherent images varies approximately as the square of the atomic number Z^2 and hence is known as Z-contrast imaging. Strong signals are obtained for heavier elements whereas lighter elements, such as O and N, may not be detected in some cases. It also becomes difficult to distinguish between elements in the image which have similar atomic numbers. However, ADF signals are highly localized at atomic positions, making them excellent indicators of atomic locations with sub-Ångström information transfer, as shown by Nellist and Pennycook [10,11].

Unambiguous identification of the atoms within an ADF image may be performed by electron energy loss spectroscopy (EELS). This detects electrons which have undergone an energy loss associated with a given inelastic scattering event and scattered through a range of angles determined by the detector geometry. To measure a particular atomic 'signature' an energy window is set about the threshold energy of a specific ionization event. Unlike ADF, EELS works well for light elements, where the energy losses of the scattered electrons are small. Since the maximum energy loss measurable by an EELS detector is a few keV, measurements are made for relatively loosely bound inner-shell electrons, which means that EELS signals are not as localized at the atomic positions as corresponding ADF signals.

Full structural and elemental composition information of the sample is acquired by correlating spectroscopic information (an EELS map) with a local structure measurement (the ADF image). However, the delocalization of the inner-shell ionization interaction can make direct correlation of the EELS signal with the probe position difficult. One aim of combining EELS data with ADF images is to investigate crystal structure via column-by-column spectroscopy [12]. This requires that the EELS signal is essentially localized to the column in question. As has recently been shown, the spreading of the probe in the crystal coupled with the delocalization of the ionization interaction, leads to EELS signals originating from neighbouring columns in addition to the column of interest [13]. Allen et al. have also shown that a similar 'cross-talk' occurs in ADF imaging [14]. Thus a probe used in column-by-column spectroscopy must produce sufficiently resolved results in both the ADF image and EELS spectra if the technique is to be feasible. It is therefore important to correctly model both the probe propagation in the sample and the underlying delocalized ionization interaction, in order to elucidate achievable resolutions in EELS spectroscopy. Simulations are required for the correct interpretation of experimental results and for the improvement of experimental procedures.

This paper discusses the extent to which the width of the probe and the detector size determines the resolution of images based on inner-shell ionization. There has been some robust debate within the field as to the extent of the delocalization of the interaction. Previous quantum mechanical descriptions have predicted both definite localization [12] and significant delocalization [15]. The results presented here are closer to those in Ref. [15]. The calculations in Ref. [12] have an incorrect modulus sign on $F(1s, 1s)$ in their Eq. (3), leading to results which are significantly too localized. The effective inelastic scattering potential for core-loss spectroscopy is nonlocal as a consequence of the use of the mixed dynamic form factor formulation and direct interpretation is complicated. If the effective scattering potential can be approximated in a suitable local form, then it can be represented in real space. The localization

is then just a measure of the peak widths. Extensive work, however, has shown the importance of the nonlocal form of the interaction and the local, or object function, approximations are not always adequate [16–19]. However, this form of scattering potential cannot be as easily visualized. In the case of zone-axis illumination, it is a function of four variables and not possible to plot or simply determine localization of the interaction by measuring the width of the potential. In order to avoid this difficulty, this paper will use the full-width at half-maximum (FWHM) of the STEM EELS images as a measure of the delocalization of the EELS interaction.

The modelling of single, isolated atoms provides an environment in which to investigate the spatial resolution for EELS imaging in STEM in a generic way, ignoring sample-dependent effects such as multiple scattering and channelling of the probe, as we have done previously [9,14,20,21]. In addition, it has been assumed that there is no thermal motion of the isolated atom, providing the optimal measure of the STEM image width, without the additional smearing due to thermal motion. However, ignoring these effects, we still expect to obtain a good qualitative feel for what one might expect for EELS imaging of a particular element, irrespective of the local environment in which it resides. The primary limitation on the width of single atom features for EELS is the width of the probe achievable in current machines [21]. This paper investigates the resolution achievable by aberration free probes, both as a function of the probe size and delocalization of the EELS interaction.

2. Theoretical background

2.1. STEM probe formation

In momentum space the wave function of a coherent STEM probe is simply the transfer function of the probe forming optics,

$$T(\mathbf{p}) = O(\mathbf{p})\exp[-\mathrm{i}\chi(\mathbf{p})], \tag{1}$$

where $\mathbf{p}$ is a transverse momentum component in the incident probe and $O(\mathbf{p})$ is the probe forming aperture pupil function. The coherent aberrations of the probe are characterized by $\chi(\mathbf{p})$,

$$\chi(\mathbf{p}) = \pi\Delta f\lambda p^2 + \frac{\pi}{2}C_s\lambda^3 p^4 + \frac{\pi}{3}C_5\lambda^5 p^6, \tag{2}$$

where $p \equiv |\mathbf{p}|$ and $\lambda \equiv 1/k$ is the wavelength of the incident electrons, k being the magnitude of the corresponding wave vector. The aberrations described in Eq. (2) are characterized by the defocus Δf (positive for overfocus) and the third and fifth order spherical aberration coefficients C_s and C_5, respectively. In this paper we will assume that all aberrations up to fifth order are corrected or perfectly balanced, i.e. $\chi(\mathbf{p}) = 0$.

The function $O(\mathbf{p})$ is a top hat function describing the allowed range of transverse momentum transfer,

$$O(\mathbf{p}) = \begin{cases} 1, & |\mathbf{p}| \leqslant p_{\max} \\ 0, & |\mathbf{p}| > p_{\max} \end{cases}. \tag{3}$$

Here $p_{\max}$ is the magnitude of the maximum transverse momentum component admitted by the aperture. The maximum transverse momentum transfer is often described in terms of the aperture semi-angle α, with $p_{\max} = k\alpha$. Consistent with common usage, we will refer to aperture dimensions in terms of α in this paper.

For most of the calculations within this paper we have chosen two standard aberration-free STEM probes formed by 300 keV incident electrons, with probe forming apertures of 10 and 20 mrad, respectively. The real space intensity profiles of these probes are shown in Fig. 1. The FWHM of the probe with an aperture of 10 mrad is approximately 1.0 Å and represents a probe size routinely achievable in a modern STEM machine fitted with an aberration corrector. The probe formed using an aperture of 20 mrad has a FWHM of approximately 0.5 Å and represents the probable probe size we can reasonably hope to attain in future machines.

2.2. STEM images for single atoms

An incoherent STEM image for inelastic scattering may be calculated in a multislice

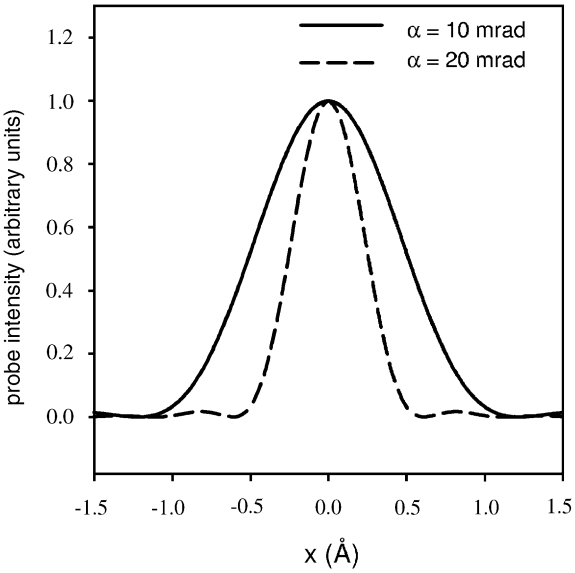

Fig. 1. Aberration free STEM probe intensities for probe forming apertures of 10 and 20 mrad, normalized to unity in each case for ease of comparison.

formulation using [14]

$$\sigma(\mathbf{R}) = \frac{1}{AV}\sum_{m=1}^{M}\left[\sum_{\mathbf{g},\mathbf{h}} \Psi^*(\mathbf{K},\mathbf{R},\mathbf{h},z_m) \times \Psi(\mathbf{K},\mathbf{R},\mathbf{g},z_m)\mu_{\mathbf{h},\mathbf{g}}\right]\Delta z_m. \quad (4)$$

The mixed dynamic form factor $\mu_{\mathbf{h},\mathbf{g}}$ in this formulation implies an effective nonlocal interaction in real space and is a generalization of previous expressions for inelastic scattering derived for plane-wave illumination [19,22]. The calculation is performed using a supercell of volume V, with area A and sums over M slices, each of thickness Δz_m. The term $\Psi(\mathbf{K},\mathbf{R},\mathbf{g},z_m)$ is the Fourier transform of the wave function in the crystal

$$\Psi(\mathbf{K},\mathbf{R},\mathbf{g},z_m) = \int_A \psi(\mathbf{K},\mathbf{R},\mathbf{r}_\perp,z_m) \times \exp(-2\pi i\mathbf{g}\cdot\mathbf{r}_\perp)\,\mathrm{d}\mathbf{r}_\perp, \quad (5)$$

where $\mathbf{K}$ is the wave vector of the incident electrons corrected for refraction and $\mathbf{R}$ denotes the probe position. The position coordinates of the wave function are expressed in terms of $\mathbf{r}_\perp$, a component perpendicular to the direction of propagation, and the depth z_m. The momentum space vectors $\mathbf{g}$ and $\mathbf{h}$ are those related to the supercell.

The terms $\mu_{\mathbf{h},\mathbf{g}}$ occurring in Eq. (4) are the inelastic scattering coefficients, which for this paper, describe the inelastic scattering due to the EELS ionization potential. The EELS ionization potential must be calculated explicitly as a function of two momentum space vectors as [18,19]

$$\mu_{\mathbf{h},\mathbf{g}} = \frac{1}{2\pi k V_c}\sum_n \exp[-M(\mathbf{h}-\mathbf{g})] \times \exp[2\pi i(\mathbf{h}-\mathbf{g})\cdot\boldsymbol{\tau}_n] f_{\mathbf{h},\mathbf{g}}. \quad (6)$$

Here V_c is the volume of the fundamental unit cell, $M(\mathbf{h}-\mathbf{g})$ is the Debye–Waller factor accounting for thermal motion of the atoms within the crystal lattice and $\boldsymbol{\tau}_n$ is the real space vector describing the position of the atomic species of interest within the unit cell. The atomic scattering factors for inner-shell ionization are given by

$$f_{\mathbf{h},\mathbf{g}} = \frac{1}{2\pi^3 a_0^2}\int k'\kappa^2\left\{\int\left[\sum_{l,m_l} n_{m_l}\int F^*_{l,m_l}(\mathbf{Q}_\mathbf{h},\boldsymbol{\kappa}) \times F_{l,m_l}(\mathbf{Q}_\mathbf{g},\boldsymbol{\kappa})\,\mathrm{d}\Omega_\kappa\right]\frac{\mathrm{d}\Omega_{k'}}{|\mathbf{Q}_\mathbf{h}|^2|\mathbf{Q}_\mathbf{g}|^2}\right\}\mathrm{d}\kappa, \quad (7)$$

where a_0 is the relativistic Bohr radius and k' is the magnitude of the wave vector $\mathbf{k}'$ of the scattered electron. The wave vector of the ejected electron is denoted by $\boldsymbol{\kappa}$ (magnitude κ). The momentum transferred to the object from the incident electron is defined by the wave vector $\mathbf{q}$, through $h\mathbf{q} = h(\mathbf{k}-\mathbf{k}')$. The quantum number l is associated with orbital angular momentum and the sum over m_l, the azimuthal quantum number, is required for initial bound states other than s-orbitals. The factor n_{m_l} takes into account the number of electrons in each sub-orbital.

The angular integration, $\mathrm{d}\Omega_{k'} = \sin\theta\,\mathrm{d}\theta\,\mathrm{d}\phi$, extends over ranges determined by the geometry of the detector. For a circular EELS detector located on the optical axis of the microscope, the θ integration is restricted to the collection semi-angle β of the detector. The energy window of the detector, ΔE, limits the range of the κ integration.

The atomic transition matrix element for a particular orbital is given by

$$F_{l,m_l}(\mathbf{Q_h}, \boldsymbol{\kappa}) = \int b^*(\boldsymbol{\kappa}, \mathbf{r}) \times \exp[2\pi \mathrm{i}\mathbf{Q_h} \cdot \mathbf{r}] u_0(\mathbf{r})\, \mathrm{d}\mathbf{r}. \quad (8)$$

Here $u_0(\mathbf{r})$ and $b(\boldsymbol{\kappa}, \mathbf{r})$ are the wave functions of the (appropriately normalized) bound and continuum states, respectively. The matrix elements are for a specific sub-orbital in an atom and are functions of $\mathbf{Q_h} = \mathbf{q} + \mathbf{h}$. The integral is calculated in the angular momentum representation [17,23,24] to allow the use of realistic atomic wave functions. Unlike previous expressions for the matrix element [25] based on a hydrogenic model, there is no limitation to K-shell ionization. The bound states are Hartree–Fock wave functions with relativistic corrections calculated using Cowan's program RCN [26] and the continuum states are described by Hartree–Slater wave functions [17,27]. To simulate the STEM EELS image of an isolated atom, we have constructed a unit cell with dimension 10 Å by 10 Å and a thickness of 2 Å, the approximate diameter of an atom [28], with a single atom sitting at the origin. The unit cell was tiled in the direction perpendicular to propagation (in the plane defined by $\mathbf{r}_\perp$) to produce an 8×8 supercell distributed over 512×512 pixels. Thermal motion has been ignored effectively giving $\mu_{\mathbf{h},\mathbf{g}} = f_{\mathbf{h},\mathbf{g}}/2\pi k V_c$. In addition, for a single atom, $K \simeq k$ so the cross-section, calculated using a single slice of thickness Δz, is given by

$$\sigma(\mathbf{R}) = \frac{1}{2\pi k V_c V A} \left[\sum_{\mathbf{g},\mathbf{h}} \Psi^*(\mathbf{K}, \mathbf{R}, \mathbf{h}, z) \times \Psi(\mathbf{K}, \mathbf{R}, \mathbf{g}, z) f_{\mathbf{h},\mathbf{g}} \right] \Delta z, \quad (9)$$

where V_c is the volume of the unit cell. The calculation of the atomic scattering factors is computationally intensive and typical calculation times for the results presented in this paper took between 19 and 34 h on an Intel XEON, 2.00 GHz machine for each atomic orbital.

3. Single atom STEM EELS imaging

Simulated STEM images were made for single, isolated atoms using an incident probe energy of 300 keV, assuming an aberration free probe. The EELS detector has a collection semi-angle $\beta = 20$ mrad and an energy window $\Delta E = 40$ eV above the threshold energy for ionization. In order to quantify the resolution obtainable with the simulated probe, the FWHM of the STEM images were calculated.

Typical images are shown in Fig. 2(a) for K-shell ionization of carbon, magnesium and calcium where a probe forming aperture $\alpha = 20$ mrad has been used. Results are normalized to a common maximum value of unity for ease of comparison. As expected, the FWHM decreases with increasing atomic number Z as the K-shell electrons become more tightly bound. As found by Kohl and Rose [15], volcano-like structures occur in inelastic single atom STEM images, especially for large probe forming apertures and small detector collection angles. As α increases, the probe size in real space becomes correspondingly smaller. When a probe is tightly focused on the atomic site, electrons tend to be scattered through large angles and hence may not be collected by the detector, leading to a deficit in the image at the atomic site. Decreasing α or increasing the detector collection angle β results in these structures disappearing. The development of a 'volcano' as a function of increasing α is illustrated in Fig. 2(b). For $\alpha = 15$ mrad the STEM image is sharply peaked. As α is increased to 20 mrad the top of the image flattens out, leading to a small increase in the FWHM. By the time $\alpha = 30$ mrad the volcano-like structure is well defined and the FWHM is reduced.

The variation of the FWHM of STEM EELS images as a function of atomic number is shown in Fig. 3(a) for K-shell ionization using apertures of $\alpha = 10$ mrad (filled circles) and $\alpha = 20$ mrad (filled triangles). Results are plotted for atomic numbers between $Z = 6$ (carbon) and $Z = 20$ (calcium). The reduction of the FWHM as a function of Z, expected due to the tighter binding of the K-shell electrons of heavier atoms, is obvious for both aperture sizes. In addition there is a substantial

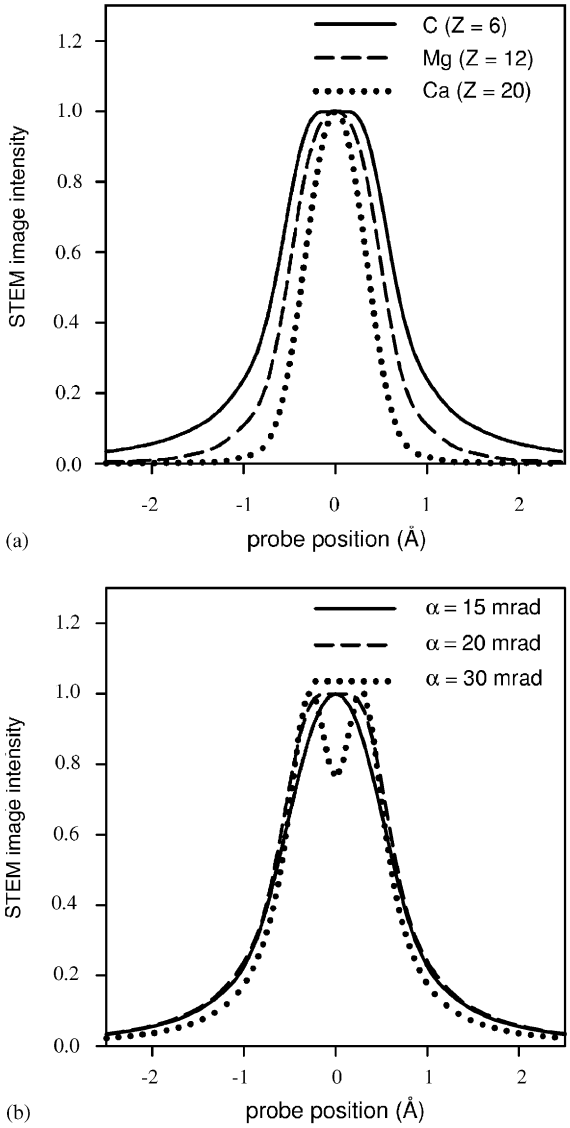

Fig. 2. (a) STEM images for the elements carbon, magnesium and calcium. The probe forming aperture is 20 mrad with an EELS detector collection semi-angle of 20 mrad and an energy window of 40 eV. (b) STEM images for the K-shell ionization of carbon showing the appearance of a 'volcano' for the larger probe forming aperture with an EELS detector semi-angle of 20 mrad.

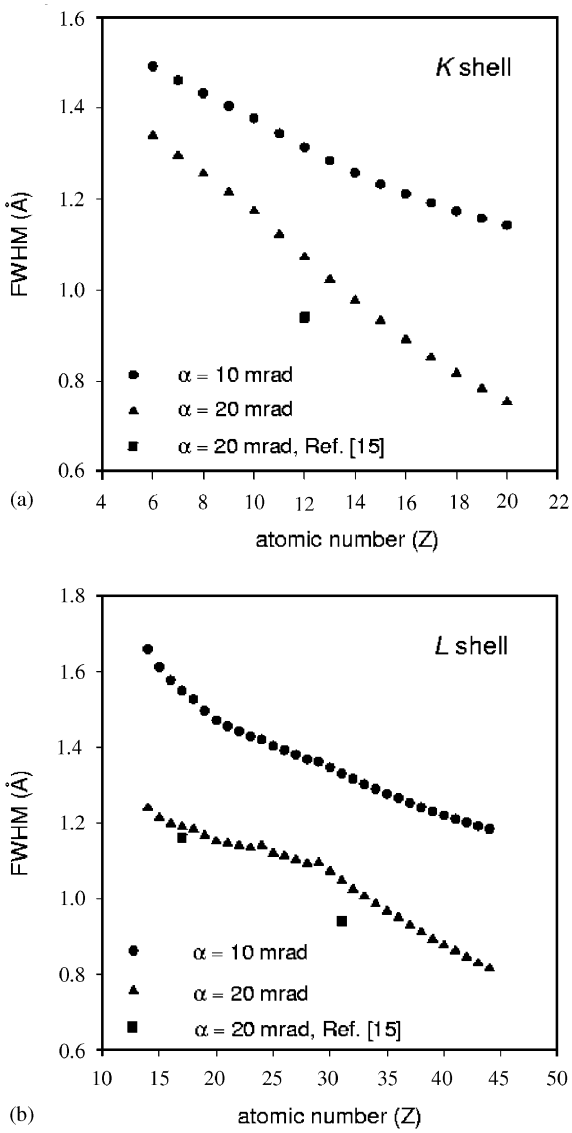

Fig. 3. FWHM of STEM core-loss images plotted as a function of atomic number for (a) K-shell ionization and (b) L-shell ionization. Results are shown for $\alpha = 10$ mrad (filled circles) and $\alpha = 20$ mrad (filled triangles). An EELS detector with collection semi-angle $\beta = 20$ mrad and energy window of $\Delta E = 40$ eV is assumed. Where possible, FWHM inferred from Ref. [15] are included for comparison (filled squares).

reduction in the FWHM of the STEM images for the STEM probe formed with the 20 mrad aperture. In the most extreme case investigated, calcium, there is a 60% decrease in the FWHM by using the larger aperture of 20 mrad. This compares to a reduction of only 10% for carbon. The smaller reduction for the carbon STEM image will be discussed at a later point.

The variation of the FWHM of L-shell STEM images with atomic number is shown in Fig. 3(b). L-shell STEM images were simulated for the elements silicon ($Z = 14$) to ruthenium ($Z = 44$). Again, the FWHM decreases with increasing atomic number and the resolution of the images is dependent upon probe size. Further, the FWHM can once again be reduced by as much as 60% (for ruthenium) by using the 20 mrad aperture.

While the FWHM of the L-shell images formed using $\alpha = 10$ mrad reduces smoothly with increasing Z, this is not the case when the probe forming aperture is 20 mrad. In particular, for chromium ($Z = 24$) and copper ($Z = 29$) the FWHM is larger than that of the elements either side in the atomic series. This is due to irregularities in the filling of the 4s and 3d states, which are similar in energy [28]. This affects the corresponding transition matrix elements in Eq. (8).

It should be noted that although the Si K-edge appears to give a higher resolution image than the L-edge, the lower signal levels in the K-edge may mean the image has an overall lower resolvability.

The FWHM of a STEM EELS image is dependent not only on the probe size, but also on the size of the EELS detector, the dependence of $f_{\mathbf{h},\mathbf{g}}$ on collection angle being explicit in Eq. (7). To investigate this dependence, the FWHM for carbon and calcium K-shell ionization has been plotted as a function of both the probe forming aperture size and the detector collection angle in Figs. 4(a) and (b), respectively. Two interesting features can be seen in the carbon FWHM plot shown in Fig. 4(a). The first is the diagonal ridge highlighted by the thick black line. This ridge represents the point at which volcano-like structures form in the STEM images. These structures occur on the large α side of the ridge. As β increases in size, electrons scattered through larger angles are detected. This leads to a more 'localized' interaction and we expect a correspondingly reduced FWHM for the STEM image. For small values of α this effect is clear. In the case of the carbon K-shell this is somewhat distorted by the volcano-formation ridge. However for $\alpha = 40$ mrad, all images have volcano-like structure, and there is a small but obvious increase in the FWHM with increasing collection angle. We believe that this is due to the fact that small collector angles lead to an interaction where the 'nonlocal nature' is enhanced [20], especially for weakly bound orbitals, and resulting in a reduction of the FWHM. This phenomenon requires greater investigation and is beyond the scope of this paper.

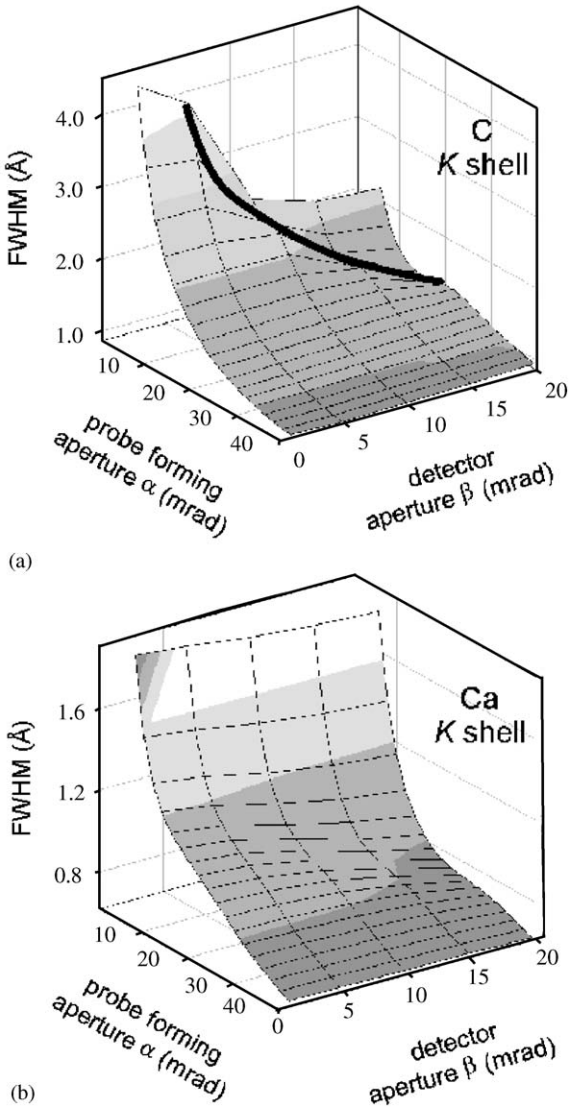

Fig. 4. Variation of the FWHM of STEM images with probe forming aperture and EELS detector semi-angle for the K-shell ionization of: (a) carbon, and (b) calcium.

The results for the FWHM of calcium K-shell STEM images, shown in Fig. 4(b) has a 'volcano ridge' that is very much smaller than that occurring in the plot for the carbon K-shell. In addition, for the more tightly bound K-shell electrons in calcium, the increase in the FWHM with increasing β for large α is not evident.

Similar plots are shown for the silicon and ruthenium L-shells in Figs. 5(a) and (b), respectively. No volcano-like structures are present in the silicon L-shell images and the apparent ridge on Fig. 5(a) is an optical illusion. Volcano-like structures do occur in the ruthenium images, but only at the upper limit of the probe forming aperture sizes plotted here. For both silicon and ruthenium, and all detector sizes, the FWHM reduces monatonically with increasing α. However, for the more weakly bound silicon L-shell, the FWHM increases with increasing β for $\alpha = 40$ mrad, we surmise for similar reasons to the carbon K-shell results in Fig. 4(a) above. The ruthenium results do not exhibit this behaviour.

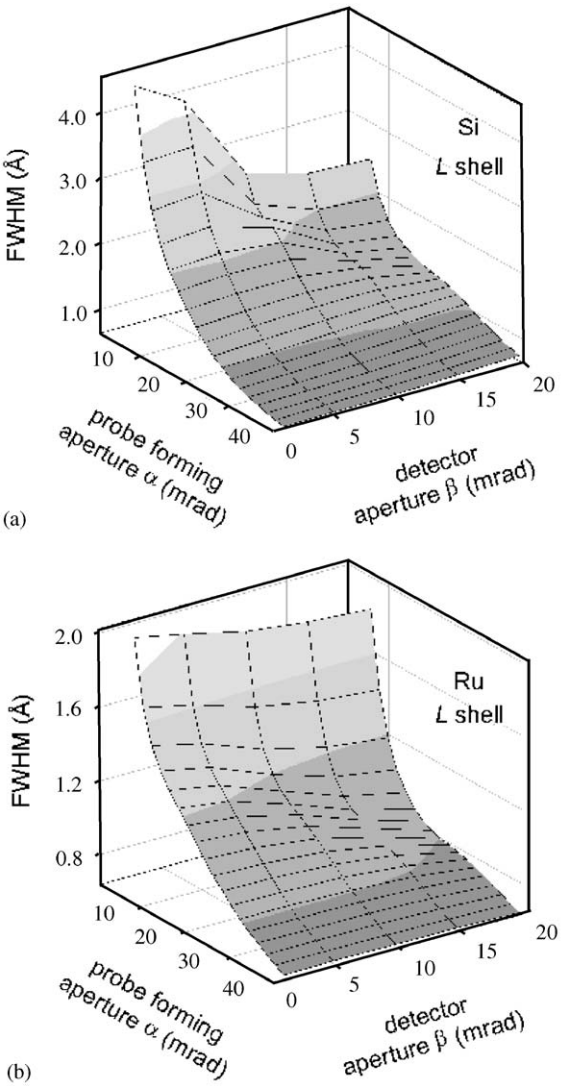

Fig. 5. Variation of the FWHM of STEM images with probe forming aperture and EELS detector semi-angle for the L-shell ionization of: (a) silicon, and (b) ruthenium.

4. Resolvability

Consider the case of the silicon dumbells as seen under $\langle 1\,1\,0 \rangle$ zone axis conditions. The atomic columns in this case are separated by 1.36 Å. Shown in Fig. 6 are the STEM core-loss images that would result from two silicon atoms separated by this distance for $\alpha = 20$ mrad and the parameters used in Fig. 3. The images of individual atoms are shown by the dotted lines and the sum of these images shown by the solid line. Fig. 6(a) shows the silicon K-shell images. The individual images have a FWHM of 0.98 Å. When separated by 1.36 Å the images merge and the minimum value between the peaks is approximately 50% of the maximum value. Such a difference should allow the resolution of the individual Si atoms. For the L-shell images shown in Fig. 6(b) (FWHM= 1.24 Å) the minimum value of the intensity between the atoms is approximately 80% of the maximum. This could make the resolution of individual atoms difficult. So the FWHM values in this paper can be considered to provide an estimated lower bound on the separation between atoms if they are to be resolved using core-loss imaging. Clearly, for the results shown in Fig. 3, the use of a 10 mrad probe forming aperture would lead to the individual atoms being merged into a single signal. It should be noted that these estimates are based on the resolution of the STEM images for single atoms and do not take into account the effects of channelling that would occur in a silicon crystal.

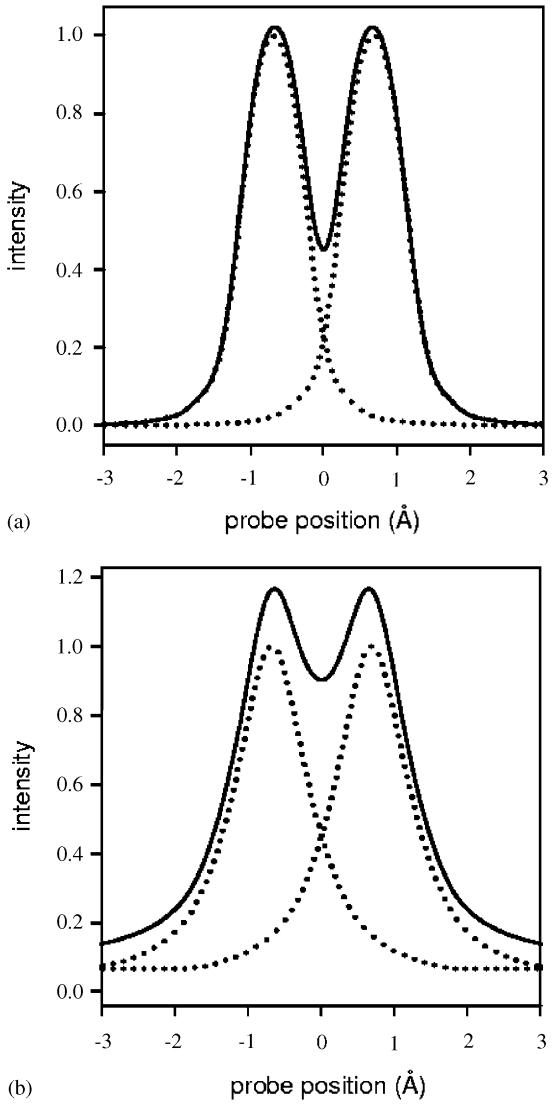

Fig. 6. Resolution of silicon dumbells for 300 keV incident electrons and a probe forming aperture of $\alpha = 20$ mrad. The EELS detector has a semi-collection angle $\beta = 20$ mrad and an energy window $\Delta E = 40$ eV above threshold. (a) Silicon K-shell, and (b) Silicon L-shell.

5. Conclusion

This paper investigated the resolution of STEM imaging, based on core-loss spectroscopy. The 'delocalization' of inelastic scattering is seen to be a crucial issue for the ultimate spatial resolution of core-loss spectroscopy in the electron microscope. Images for single atoms were simulated from first principles using a nonlocal model for electron core-loss spectroscopy. The role of the width of the probe, relative to the delocalization of the underlying ionization interaction has been elucidated. The results indicate that, with future advances in electron microscopy, column-by-column spectroscopy of crystal samples using core-loss spectroscopy will be a feasible procedure.

Acknowledgements

The authors acknowledge fruitful discussions with Scott Findlay. M.P. Oxley and L.J. Allen acknowledge support by the Australian Research Council. S.J. Pennycook acknowledges support by the Laboratory Directed Research and Development Program of ORNL, managed by UT-Battelle, LLC, for the US Department of Energy under Contract no. DE-AC05-00OR22725.

References

[1] S.J. Pennycook, A.R. Lupini, A. Kadavanich, J.R. McBride, S.J. Rosenthal, R.C. Puetter, A. Yahil, O.L. Krivanek, N. Dellby, P.D. Nellist, G. Duscher, L.G. Wang, S.T. Pantelides, Z. Metallk. 94 (2003) 350.
[2] R.D. Leapman, J. Microsc. 210 (2003) 5.
[3] N. Dellby, O.L. Krivanek, P.D. Nellist, P.E. Batson, A.R. Lupini, J. Electron Microsc. 50 (2001) 177.
[4] P.E. Batson, N. Dellby, O.L. Krivanek, Nature 418 (2002) 617.
[5] A.R. Lupini, S.J. Pennycook, Ultramicroscopy 96 (2003) 313.
[6] URL http://www.superstem.dl.ac.uk.
[7] URL http://ncem.lbl.gov/team3.htm.
[8] P.M. Voyles, D.A. Muller, J.L. Grazul, P.H. Citrin, H.-J.L. Gossmann, Nature 416 (2002) 826.
[9] M. Varela, S.D. Findlay, A.R. Lupini, H.M. Christen, A.Y. Borisevich, N. Dellby, O.L. Krivanek, P.D. Nellist, M.P. Oxley, L.J. Allen, S.J. Pennycook, Phys. Rev. Lett. 92 (2004) 095502.
[10] P.D. Nellist, S.J. Pennycook, Ultramicroscopy 78 (1999) 111.
[11] P.D. Nellist, S.J. Pennycook, Phys. Rev. Lett. 81 (1998) 4156.
[12] B. Rafferty, S.J. Pennycook, Ultramicroscopy 78 (1999) 141.
[13] C. Dwyer, J. Etheridge, Ultramicroscopy 96 (2003) 343.
[14] L.J. Allen, S.D. Findlay, M.P. Oxley, C.J. Rossouw, Ultramicroscopy 96 (2003) 47.

[15] H. Kohl, H. Rose, Adv. Imaging Electron. Phys. 65 (1985) 173.
[16] M.P. Oxley, L.J. Allen, Acta Crystallogr. A 56 (2000) 470.
[17] M.P. Oxley, L.J. Allen, Phys. Rev. B 57 (1998) 3273.
[18] M.P. Oxley, L.J. Allen, Acta Crystallogr. A 57 (2001) 713.
[19] L.J. Allen, T.W. Josefsson, Phys. Rev. B 52 (1995) 3184.
[20] C.J. Rossouw, L.J. Allen, S.D. Findlay, M.P. Oxley, Ultramicroscopy 96 (2003) 299.
[21] L.J. Allen, S.D. Findlay, A.R. Lupini, M.P. Oxley, S.J. Pennycook, Phys. Rev. Lett. 91 (2003) 105503.
[22] L.J. Allen, T.W. Josefsson, Phys. Rev. B 53 (1996) 11285.
[23] S.T. Manson, Phys. Rev. A 6 (1972) 1013.
[24] D.K. Saldin, P. Rez, Philos. Mag. B 55 (1987) 481.
[25] V.W. Maslen, C.J. Rossouw, Philos. Mag. A 47 (1983) 119.
[26] R.D. Cowan, The Theory of Atomic Structure and Spectra, University of California Press, Berkeley, 1981.
[27] F. Herman, S. Skillman, Atomic Structure Calculations, Prentice-Hall, Englewood Cliffs, NJ, 1963.
[28] B.H. Bransden, C.J. Joachain, Physics of Atoms and Molecules, Longman, Essex, 1999.